Enhance the Performance of Dye-Sensitized Solar Cells by Co-grafting Amphiphilic Sensitizer and Hexadecylmalonic Acid on TiO₂ Nanocrystals

Peng Wang, Shaik M. Zakeeruddin,* Pascal Comte, Raphael Charvet, Robin Humphry-Baker, and Michael Grätzel*

Laboratory for Photonics and Interfaces, Swiss Federal Institute of Technology Lausanne (EPFL), CH 1015, Lausanne, Switzerland

Received: September 1, 2003; In Final Form: October 23, 2003

Dye-sensitized solar cells have been fabricated based on nanocrystalline TiO₂ film derivatized with an amphiphilic polypyridyl ruthenium complex, *cis*-RuLL′(SCN)₂ (L = 4,4′-dicarboxylic acid-2,2′-bipyridine, L′ = 4,4′-dinonyl-2,2′-bipyridine), as light-harvester and hexadecylmalonic acid (HDMA) as coadsorbent. The cells generated a short-circuit photocurrent of 15.2 mA cm^{-2}, an open-circuit photovoltage of 764 mV, and a total power conversion efficiency of 7.8% under simulated full sunlight (air mass 1.5, 100 mW cm^{-2}). Co-grafting enhanced the photocurrent, photovoltage, and overall conversion efficiency considerably with respect to cells containing no HDMA. Devices showed a good stability under light soaking at 55 °C.

Introduction

During the past decade, dye-sensitized solar cells (DSCs) have attracted much attention as low-cost alternatives to conventional inorganic photovoltaic devices.[1−4] The mesoscopic TiO₂ film texture in these cells significantly increases the cross section for surface-anchored light-harvesters while maintaining a good contact with electrolytes. In these devices, photon-to-electricity conversion is achieved by ultrafast electron-injection from a photoexcited dye into the conduction band of TiO₂ and subsequently dye regeneration and hole transportation to the counter electrode. An impressive 10.4% solar-to-electric power conversion efficiency has been achieved with a DSC. However, the achievement of long-term stability, which is an important requirement for the application of DSCs, has become a major challenge for a long time.

The leakage of organic solvent from such modules, possible desorption of loosely attached dyes, and photodegradation in the desorbed state as well as corrosion of the Pt counter electrode by the triiodide/iodide couple have been suggested as some critical factors limiting the long-term performance of DSCs, especially at elevated temperature. Thus considerable efforts have been undertaken to realize devices with high efficiencies that meet the stability criteria for practical use.[5,6] In this context, new counter electrode materials,[7−9] alternative redox couples,[10−12] and sensitizers[13−21] have been screened. Additionally, *p*-type semiconductor,[22,23] hole-conductor,[24,25] and polymeric or gel materials[26−30] incorporating triiodide/iodide as a redox couple were introduced to substitute the liquid electrolytes by solid-state or quasi-solid-state materials. A quasi-solid electrolyte composed of 2,3-dimethyl-1-propyl imidazolium iodide (DMPII), 3-methoxypropionitrile (MPN), *N*-methylbenzimidazole (NMBI), and a fluorinated polymer was recently introduced. When used in conjunction with an amphiphilic derivative of the ruthenium dye Z-907 (Figure 1), it provided remarkably stable performance under long-term light soaking at 55 °C and thermal stress at 80 °C, albeit at a lower efficiency level of 6%.[31]
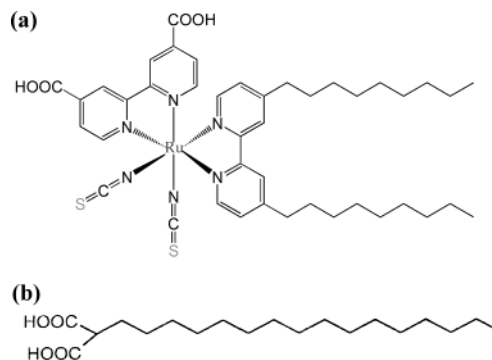
* Authors to whom correspondence should be addressed. E-mail: shaik.zakeer@epfl.ch; michael.graetzel@epfl.ch.

Figure 1. Molecular structures of (a) Z-907 dye and (b) HDMA coadsorbent.

In this paper, a modified electrolyte with the ionic liquid 1-methyl-3-propylimidazolium iodide (PMII) as iodide resource instead of the solid DMPII allows an increase in the conversion efficiency from 6.2 to 7.2%. A further remarkable increase in photovoltaic performance was achieved by co-grafting hexadecylmalonic acid (HDMA, Figure 1) with Z-907 sensitizer onto nanocrystalline TiO₂ film. Like Z-907, HDMA contains two carboxylate groups to anchor it on the TiO₂ surface. Co-grafting of the two amphiphiles will result in the formation of a mixed monolayer which should be more tightly packed than when the sensitizer is adsorbed alone, providing a more effective insulating barrier for the back electron transfer from TiO₂ conduction band to triiodide in the electrolyte. Retarding this unwanted redox process by the hydrophobic spacer will reduce the dark current and increase the open circuit voltage of the solar cell. The device also showed good stability under light soaking at 55 °C in simulated sunlight.

Experimental Section

Reagents and Electrolytes. Tetrabutylammonium hexafluorophosphate (TBAPF₆), iodine, acetic acid, nitric acid, titanium iso-propoxide, ethyl cellulose, terpineol, ethanol, and HDMA were used as received from Fluka, Aldrich or Lancaster. NMBI was purchased from Aldrich and recrystallized from diethyl

ether. MPN (Fluka) was distilled before use. The amphiphilic Z-907 dye [cis-Ru(H$_2$dcbpy)(dnbpy)(NCS)$_2$, where the ligand H$_2$dcbpy is 4,4′-dicarboxylic acid-2,2′-bipyridine and dnbpy is 4,4′-dinonyl-2,2′-bipyridine] was synthesized as described in our previous paper.[31] PMII was prepared according to the literature method[32] and confirmed by ^{1}H NMR spectrum. TiO$_2$ particles (400-nm-sized) were received as a gift from CCIC (Japan). The new electrolyte is composed of 0.6 M PMII, 0.1 M I$_2$, and 0.45 M NMBI in MPN solvent.

Preparation and Characterization of 20-nm-Sized TiO$_2$ Colloid. An amount of 12 g (0.2 mol) of acetic acid was added dropwise to 58.6 g (0.2 mol) of titanium iso-propoxide under stirring at room temperature. The modified precursor was stirred for about 15 min and poured into 290 mL water as fast as possible with vigorous stirring (700 rpm). A white precipitate was instantaneously formed. One hour stirring was performed to achieve a complete hydrolysis reaction. After adding a quantity (5.4 mL for sample A; 4 mL for sample B) of 65% nitric acid, the mixture was heated from room temperature to 78 °C within 40 min and peptized for 75 min. Then, water was added to the cooling liquid mixture to adjust the volume to be 370 mL. The resultant mixture was kept in a 570 mL titanium autoclave and heated at 250 °C for 12 h. After that, 2.4 mL of 65% nitric acid was added and dispersed with a 200 W ultrasonic titanium probe at a frequency of 15 pulses every second. The resultant colloidal solution was concentrated with a rotary-evaporator to contain 18% TiO$_2$. Finally, it was centrifuged to remove nitric acid and washed with ethanol three times to produce a colloidal solution containing 40% TiO$_2$ and 4% water in ethanol. X-ray diffraction (XRD) patterns were recorded using a powder diffractometer (Scintag, USA) with Cu Kα radiation. For the observation of synthesized particles by SEM (Hitachi S-900), a drop of the final TiO$_2$ colloid was further diluted with ethanol and then spread on a holey amorphous carbon film deposited on Ni grid.

Preparation of Screen-Printing Pastes. The TiO$_2$ colloid in ethanol was mixed with terpineol and a solution of ethyl cellulose in ethanol. After removing ethanol and water with a rotary-evaporator, paste A consisting of 16.2% 20-nm-sized TiO$_2$ (sample A) and 4.5% ethyl cellulose in terpineol was prepared. Paste B is composed of 28.6% 400-nm-sized TiO$_2$ and 7.2% ethyl cellulose in terpineol.

Preparation and Characterization of Double-Layer TiO$_2$ Electrode. The fluorine-doped SnO$_2$ conducting glass was first cleaned in Triton X-100 aqueous solution, washed with ethanol, and treated with 50 mM TiCl$_4$ aqueous solution at 70 °C for 30 min in order to make a good mechanical contact between the following printed TiO$_2$ layer and conducting glass matrix. Then, a transparent film of 20-nm-sized TiO$_2$ particles was printed on the TiCl$_4$-treated conducting glass with paste A and further coated by the second layer of 400 nm light scattering anatase particles with paste B. The screen-printed double-layer was gradually heated to 500 °C under oxygen and subsequently left for sintering. The programmed heating procedure is described in Supporting Information. After treatment with 40 mM TiCl$_4$ again, the as-prepared double-layer nanocrystalline film was rinsed with water and ethanol and stored in dry air for device fabrication. The layer thickness was determined by Alpha-step 200 surface profilometer (Tencor Instruments, USA). The final thickness for the transparent layer is 10 μm and that for the scattering layer is 4 μm. The porosity and average pore size of the transparent layer were measured with a Gemini 2327 nitrogen adsorption apparatus (Micromeretics Instrument Corp., USA) to be 63% and 22 nm, respectively.

Fabrication of Dye-Sensitized Solar Cells. After sintering at 500 °C and cooling to 80 °C, the double-layer nanostructured TiO$_2$ electrodes were dye-coated by immersing them into dye solutions at room temperature for 12 h and then assembled with thermally platinized conducting glass electrodes. While dye solution A consisted of 300 μM Z-907 dye in acetonitrile and *tert*-butyl alcohol (volume ratio: 1:1), solution B contained 300 μM Z-907 dye and 75 μM HDMA as coadsorbent. The electrodes were separated by a 35 μm thick Bynel hot-melt ring (DuPont, USA) and sealed up by heating. The internal space was filled with electrolyte using a vacuum pump to produce device A without HDMA coadsorbent and device B with HDMA. The electrolyte-injecting hole made with a sandblasting drill on the counter electrode glass substrate was sealed with a Bynel sheet and a thin glass cover by heating. After all these procedures, the cells were stored in the oven for heating posttreatment at 55 °C for 4 h and cooled to room temperature before photoelectrochemical measurements.

ATR-FTIR and UV−Vis Measurements. The spectra were measured using a FTS 7000 FTIR spectrometer (Digilab, USA). The data reported here were taken with the "Golden Gate" diamond anvil ATR accessory. Spectra were derived from 64 scans at a resolution of 2 cm^{-1}. The samples were measured under the same mechanical force pushing the samples in contact with the diamond window. No ATR correction has been applied to the data. It also has to be appreciated that this ATR technique probes at most 1 μm of sample depth and that this depends on the sample refractive index, porosity, etc. Some of the spectra show artifacts due to attenuation of light by the diamond window in the 2000 to 2350 cm^{-1} region. The coated films were rinsed in acetonitrile and dried prior to measuring the spectra. UV−vis spectra were on a Cary 5 spectrophotometer.

Electrochemical Measurements. A computer-controlled Autolab P20 electrochemical workstation (Eco Chimie, Netherlands) was employed for voltammetric measurements. A 2.5 μm thick TiO$_2$ nanocrystalline film on conducting glass was dye-coated and used as working electrode to study the electrochemical behavior of Z-907 on TiO$_2$ nanocrystals. A Pt foil and an Ag/AgCl/KCl$_{sat}$ were used as counter and reference electrodes, respectively. A two-electrode electrochemical cell, consisting of a 5.0 μm radius Pt ultramicroelectrode (Bioanalytical Systems, Inc., USA) as working electrode and a Pt foil as counter electrode, was used for the diffusion coefficient measurements of triiodide and iodide. A CDM210 conductivity meter (Radiometer Analytical, France) was employed to measure the conductivities of our electrolyte at various temperatures. The CDC749 conductivity cell (Radiometer Analytical, France) with a nominal cell constant of 1.70 cm^{-1} was calibrated with 0.1 M KCl aqueous solution prior to experiments. A DT Hetotherm cycle heat pump (Heto, Denmark) was used to control the temperature of electrolyte.

Photoelectrochemical Measurements. A 450 W xenon light source (Oriel, USA) was used to give an irradiance of 100 mW cm^{-2} (the equivalent of one sun at AM 1.5) at the surface of solar cells. The spectral output of the lamp was matched in the region of 350−750 nm with the aid of a Schott K113 Tempax sunlight filter (Präzisions Glas & Optik GmbH, Germany) so as to reduce the mismatch between the simulated and true solar spectra to less than 2%. Various incident light intensities were regulated with neutral wire mesh attenuators. The current−voltage characteristics of the cell under these conditions were obtained by applying external potential bias to the cell and measuring the generated photocurrent with a Keithley model 2400 digital source meter (Keithley, USA). This process was
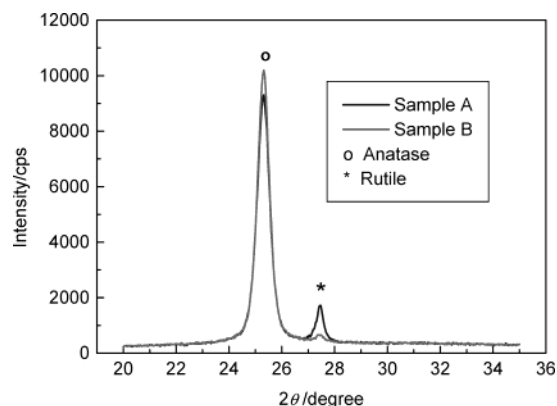
Figure 2. Powder XRD patterns of acidic TiO_2 nanocrystals (samples A and B).
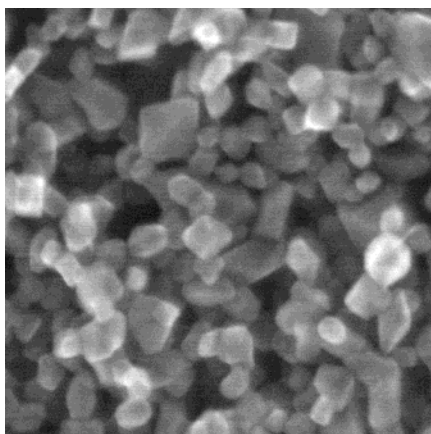

Figure 3. SEM photograph of acidic TiO_2 nanocrystals (sample B). The width of this picture is 210 nm.

fully automated using Wavemetrics software (http://www.wavemetrics.com/).

Stability Tests. Hermetically sealed cells were used for long-term stability tests under moderate thermal stress and visible light soaking. The cells covered with a 50 μm thickness of polyester film (Preservation Equipment Ltd, UK) as a UV cutoff filter (up to 400 nm) were irradiated at open circuit under a Suntest CPS plus lamp (ATLAS GmbH, 100 mW cm^{-2}, 55 °C).

Results and Discussion

Characterization of TiO_2 Nanoparticles. Figure 2 shows powder XRD patterns of TiO_2 samples. The characteristic brookite (121) peak was not observed. The phase contents of the samples were calculated from the relative peak intensities of anatase (101) and rutile (110) for bicrystalline anatase and rutile phases. In sample A, the content of rutile is 7% but only 0.4% for sample B. The relatively lower usage amount of nitric acid efficiently inhibits the formation of the rutile phase. The SEM photography of acidic TiO_2 nanoparticles (sample B) is presented in Figure 3. The mean particle diameter is 19.6 nm with a standard deviation of 6.3 nm for 177 particles.

ATR-FTIR and Electronic Spectra. Figure 4A shows ATR-FTIR spectra of a mesoporous TiO_2 film derivatized with Z-907 alone and with a mixed monolayer of Z-907 and HDMA. Spectrum (a) was obtained from films stained with dye solution A containing only the Z-907 sensitizer. The single feature at 2101 cm^{-1} arises from the thiocyanato group, the signals at 1607 and 1379 cm^{-1} are due to the symmetric and asymmetric stretching modes of carboxylate groups, and the peaks observed at 2925 and 2855 cm^{-1} correspond to the asymmetric and
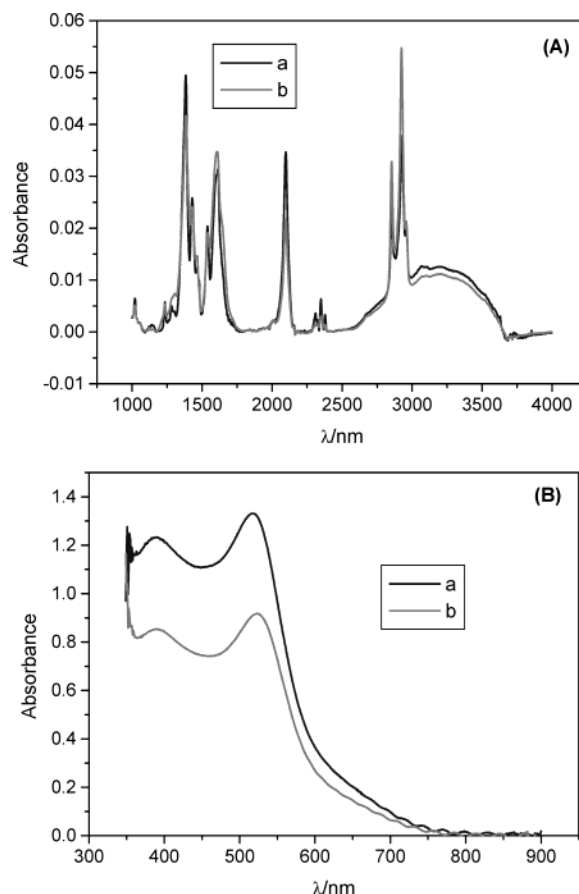

Figure 4. (A) ATR-FTIR spectra for 6.5 μm thick mesoporous TiO_2 film coated with (a) Z-907 dye alone and (b) Z-907 dye and HDMA coadsorbent. A TiO_2 reference film heated to 500 °C has been subtracted for clarity. (B) Electronic spectra for 6.5 μm thick mesoporous TiO_2 film coated with (a) Z-907 dye alone and (b) Z-907 dye and HDMA coadsorbent.

symmetric stretching modes of the CH$_2$-units of the aliphatic chains. The sharp peaks located at 1537 and 1429 cm^{-1} are ascribed to bipyridyl modes while the large broad absorption centered at 3370 cm^{-1} is due to adsorbed moisture presumably from the dye solution since the TiO_2 film is heated prior to staining. Spectrum (b) was recorded for the film stained from solution B containing both Z-907 and HDMA. The characteristic peak of the thiocyanato group of Z-907 dye has a 30% decrease, which is in consistence with the measurements of electronic spectra (Figure 4B). However, the peaks at 2925 and 2855 cm^{-1} for the asymmetric and symmetric stretching modes of the CH$_2$-units have been obviously enhanced. Furthermore, we did not observe any signal at 1700 cm^{-1} for the malonic acid headgroup of HDMA while the signals for carboxylate group increased slightly. These data confirm that HDMA has been co-grafted onto TiO_2 nanocrystals with Z-907.

Voltammetric Behavior of Z-907 Dye. Figure 5 shows typical cyclic voltammograms of 2.5 μm thick TiO_2 nanocrystalline film coated conducting glass electrode co-grafted with Z-907 and HDMA in a MPN solution containing 0.1 M TBAPF$_6$ as supporting electrolyte. When the potential is scanned between −0.2 and 1.15 V, chemically reversible redox waves with the formal potential, $(E_{ox} + E_{red})/2$, at 0.67 V are observed, which can be attributed to the one-electron oxidation and reduction of ruthenium center of Z-907 dye because neither HDMA nor TiO_2 nanocrystalline film coated conducting glass has electroactivity in the investigated potential range. Without HDMA coadsorbent, an identical formal potential value is obtained for the redox of
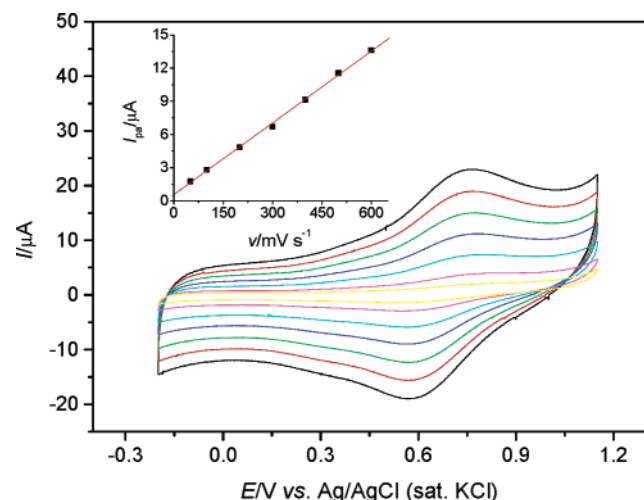
Enhance the Performance of Dye-Sensitized Solar Cells

J. Phys. Chem. B, Vol. 107, No. 51, 2003 **14339**

Figure 5. Cyclic voltammograms of Z-907 dye anchored on 2 μm TiO$_2$ nanocrystalline film with HDMA as coadsorbent. Scan rates (from inter to outer): 50, 100, 200, 300, 400, 500, and 600 mV s^{-1}, respectively. The inset shows the dependence of anodic peak currents on scan rates.

Z-907 anchored on mesoporous TiO$_2$ film. The anodic and cathodic peak potentials shift symmetrically, resulting in a constant formal potential at various scan rates. As shown in the inset of Figure 5, the anodic peak currents (I_{ap}) are linearly proportional to the scan rate (v), indicating a surface-confined electrochemical process. Besides the uncompensated ohmic drop, the nonzero peak splitting can also arise from two other basic causes.[33] First, the solvation of the redox center or the structure of co-grafted monolayer may change with the oxidation state of ruthenium center. Examples include the formation of strong ion pairs between oxidized dye molecules and hexafluorophosphate anions, and a main change in the hydrophobicity/hydrophilicity of the redox center as a function of its oxidation state. Second, the path between the two oxidation states in a free energy versus reaction coordinate plot may have an "N" shape arising from a phase change in the monolayer.[34] Additionally, the anodic and cathodic peak currents are almost the same even at the scan rate of 50 mV s^{-1}, indicating the oxidized state of Z-907 dye anchored on TiO$_2$ nanocrystals is stable for at least 10 s.

Electrolyte Conductivity. The conductivity (σ) of electrolyte employed in this study was first examined. It provides information on the mobility of the ions, their interaction with the solvent and on ion pairing phenomena, which are expected to affect the photovoltaic performance and in particular the fill factor of DSCs. Replacing DMPII used in our previous electrolyte with PMII results in a new electrolyte with room-temperature conductivity increasing from 10.4[31] to 12.0 mS cm^{-1} due to weaker ion-pairing and thus faster diffusion of ions. As is apparent from the inset of Figure 6, the Arrhenius equation cannot be used to describe the conductivity–temperature behavior of our electrolyte. A better fit to the data (Figure 6) is obtained by the Vogel–Tamman–Fulcher (VTF) equation:[35]

$$\sigma(T) = AT^{-1/2} \exp[-B/(T - T_0)] \tag{1}$$

In eq 1, A and B are constants, T is the absolute temperature, while T_0 is the glass-transition temperature. The linear-sweep voltammogram of a Pt ultramicroelectrode in this MPN-based electrolyte at a scan rate of 10 mV s^{-1} is shown in Figure 7. Anodic and cathodic currents are not affected by scan rates up to 500 mV s^{-1}, suggesting that steady-state currents controlled
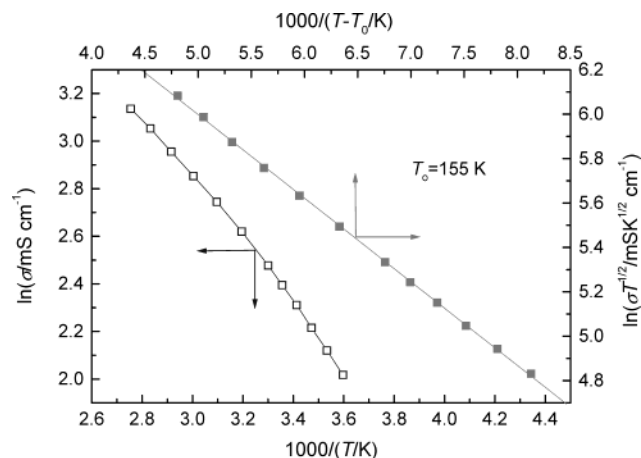

Figure 6. Plots of conductivity–temperature data of the MPN-based electrolyte in the Arrhenius and VTF coordinates.
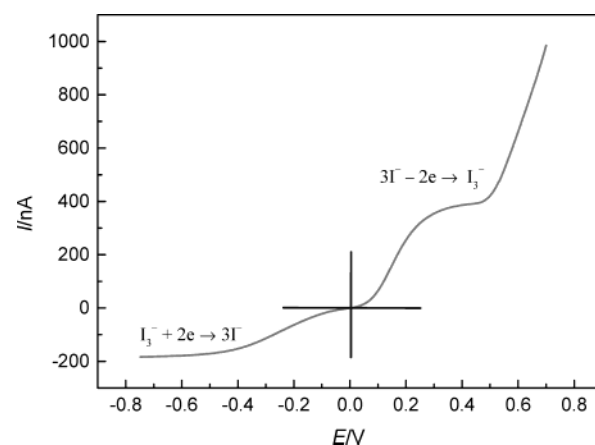

Figure 7. Steady-state voltammogram of a Pt ultramicroelectrode in the MPN-based electrolyte. Scan rate: 10 mV s^{-1}.

TABLE 1: Device Efficiencies at Varied Sunlight Irradiation

	η (%) at different incident light intensities[a]			
device	0.01 sun	0.1 sun	0.5 sun	1.0 sun
A	7.2	7.6	7.7	7.2
B	8.6	8.7	8.4	7.8

[a] The spectral distribution of the lamp mimics air mass 1.5 solar light. 1.0 Sun corresponds to an intensity of 100 mW cm^{-2}.

by the diffusion of iodide and triiodide have been attained. Thus, the apparent diffusion coefficients (D_{app}) of iodide and triiodide can be calculated from anodic and cathodic steady-state currents (I_{ss}) according to the following equation:[36]

$$I_{ss} = 4ncaFD_{app} \tag{2}$$

where n is the electron transfer number per molecule, F is the Faraday constant, and c is the bulk concentration of electroactive species. The calculated apparent diffusion coefficients of triiodide and iodide in this electrolyte are 4.2×10^{-6} and 5.4×10^{-6} cm^2 s^{-1}, respectively, 12% higher than those in our previous electrolyte.[31]

Photovoltaic Performance. The overall power conversion efficiencies at different light intensities are listed in Table 1. Figure 8 presents the current density–voltage curves for devices A and B under full sun illumination (air mass 1.5, 100 mW cm^{-2}) and in the dark. For device A, the short-circuit photocurrent density (J_{sc}), open-circuit voltage (V_{oc}), and fill factor

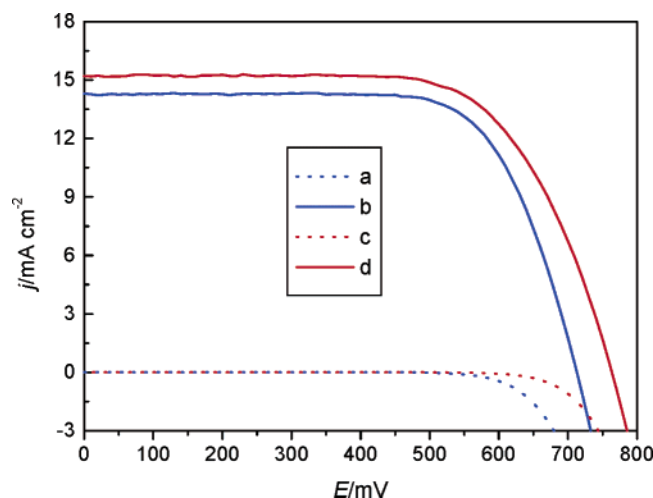**14340** *J. Phys. Chem. B, Vol. 107, No. 51, 2003*

Wang et al.

Figure 8. Photocurrent−voltage characteristics of (a) device A and (b) device B under AM 1.5 sunlight (100 mW cm^{-2}) illumination. Curves (c) and (d) were recorded in the dark for devices A and B, respectively.

(ff) are 14.2 mA cm^{-2}, 713 mV, and 0.708, respectively, yielding an overall conversion efficiency (η) of 7.2%. This is significantly higher than the 6% achieved in our previous work[31] due to the replacement of DPMII by the ionic liquid PMII. This improvement is ascribed to higher electrolyte conductivity and decreased ion pairing in the PMII compared to the DMPII-containing electrolyte. The weaker interaction of the PMI cations with iodide counterions is apparent from the fact that the PMII is a liquid down to −55 °C while DMPII is a solid at room temperature. For cells using mixed Z-907/HDMA monolayer (device B), the corresponding photovoltaic parameters (J_{sc}, V_{oc}, ff, and η) are 15.2 mA cm^{-2}, 764 mV, 0.676, and 7.8%, respectively. Thus the introduction of the HMDA cosurfactant increases J_{sc}, V_{oc}, and η while the ff decreases slightly.

The 51 mV increase in the open circuit photovoltage induced by the coadsorption of HDMA along with the amphiphilic ruthenium sensitizer Z-907 is due to suppression of the dark current arising from the reduction of triiodide by conduction band electrons. This behavior is explained by the diode equation:[37−39]

$$V_{oc} = (nRT/F) \ln[(J_{sc}/J_o) - 1] \tag{3}$$

where n is the ideality factor whose value is between 1 and 2, J_{sc} and J_o are the photocurrent under short circuit and the reverse saturation current, respectively, and R and F are the ideal gas and Faraday constants, respectively. This can be clearly seen from the dark-current measurements shown in Figure 8, where the onset potential for the reduction of triiodide shifts negatively by more than 50 mV after co-grafting.

The increase in the short circuit photocurrent may appear surprising in view of the dilution of the sensitizer by the co-grafted HDMA that should decrease the light-harvesting capacity of the mesoporous films and hence decrease the J_{sc} value. However, the mixed Z-907/HDMA monolayer appears to be sufficiently robust to impair the escape of photoinjected electrons to the electrolyte, which has been indicated by the dark current measurements. These effects appear to override the losses due to decreased light harvesting.

Device Stability. Device B showed an excellent photostability when submitted to accelerated testing in a solar simulator at a 100 mW cm^{-2} intensity. After 1000 h of light soaking at 55 °C, the drop of device efficiency is less than 10% (Figure 9)
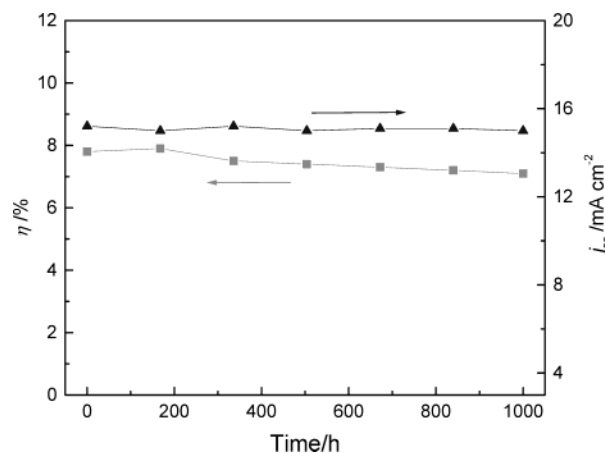

Figure 9. Power conversion efficiencies and photocurrent densities of device B during successive one sun visible-light soaking at 55 °C.

for cells covered with a UV absorbing polymer film. The decrease in efficiencies is mainly due to the gradual drop of photovoltages while photocurrents are very stable. The photovoltage drop after aging may be ascribed to the positive shift of quasi Fermi level of mesoporous anatase semiconductor. The efficiency difference (from 7.8 to 7.5) for devices tested with and without the polymer film was less than 4% at AM 1.5 sunlight, indicating a very small sacrifice in efficiency due to UV filter.

Conclusions

In conclusion, we have demonstrated that co-grafting an amphiphilic ruthenium dye with hexadecylmalonic acid onto TiO$_2$ semiconductor nanocrystals remarkably enhanced the photocurrent, photovoltage, and power conversion efficiency of dye-sensitized solar cells. For the first time, long-term stable DSCs with about 8% power conversion efficiency have been fabricated. Further studies are in progress to understand the detailed mechanism of the enhancement of photovoltaic performance due to self-assembly of mixed monolayer containing amphiphilic sensitizers and surfactant. The high contact area of the junction nanocrystalline solar cells renders the understanding and control of interfacial effects essential for future improvement of cell performance.

Supporting Information Available: Programmed heating procedure for sintering double-layer films. This material is available free of charge via the Internet at http://pubs.acs.org.

References and Notes

(1) O'Regan, B.; Grätzel, M. *Nature* **1991**, *353*, 737−740.
(2) Hagfeldt, A.; Grätzel, M. *Chem. Rev.* **1995**, *95*, 49−68.
(3) Hagfeldt, A.; Grätzel, M. *Acc. Chem. Res.* **2000**, *33*, 269−277.
(4) Grätzel, M. *Nature* **2001**, *414*, 338−344.
(5) Hinsch, A.; Kroon, J. M.; Kern, R.; Uhlendorf, I.; Holzbock, J.; Meyer, A.; Ferber, J. *Prog. Photovoltaics* **2001**, *9*, 425−438.
(6) Pettersson, H.; Gruszecki, T.; Johansson, L. H.; Johander, P. *Sol. Energy Mater. Sol. Cells* **2003**, *77*, 405−413.
(7) Kay, A.; Grätzel M. *Sol. Energy Mater. Sol. Cells* **1996**, *44*, 99−117.

(8) Saito, Y.; Kitamura, T.; Wada, Y.; Yanagida, S. *Chem. Lett.* **2002**, 1060−1061.

(9) Suzuki, K.; Yamaguchi, M.; Kumagai, M.; Yanagida, S. *Chem. Lett.* **2003**, 28−29.

(10) Nusbaumer, H.; Moser, J. E.; Zakeeruddin, S. M.; Nazeeruddin, M. K.; Grätzel, M. *J. Phys. Chem. B* **2001**, *105*, 10461−10464.

(11) Sapp, S. A.; Elliott, C. M.; Contado, C.; Caramori, S.; Bignozzi, C. A. *J. Am. Chem. Soc.* **2002**, *124*, 11215−11222.

(12) Nusbaumer, H.; Zakeeruddin, S. M.; Moser, J. E.; Grätzel, M. *Chem. Eur. J.* **2003**, *9*, 3756−3763.

(13) Nazeeruddin, M. K.; Kay, A.; Rodicio, I.; Humphry-Baker, R.; Muller, E.; Liska, P.; Vlachopoulos, N.; Grätzel, M. *J. Am. Chem. Soc.* **1993**, *115*, 6382−6390.

(14) Monat, J. E.; McCusker, J. K. *J. Am. Chem. Soc.* **2000**, *122*, 4092−4097.

(15) Nazeeruddin, M. K.; Péchy, P.; Renouard, T.; Zakeeruddin, S. M.; Humphry-Baker, R.; Comte, P.; Liska, P.; Cevey, L.; Costa, E.; Shklover, V.; Spiccia, L.; Deacon, G. B.; Bignozzi, C. A.; Grätzel, M. *J. Am. Chem. Soc.* **2001**, *123*, 1613−1624.

(16) He, J. J.; Benko, G.; Korodi, F.; Polivka, T.; Lomoth, R.; Akermark, B.; Sun, L. C.; Hagfeldt, A.; Sundstrom, V. *J. Am. Chem. Soc.* **2002**, *124*, 4922−4932.

(17) Renouard, T.; Fallahpour, R. A.; Nazeeruddin, M. K.; Humphry-Baker, R.; Gorelsky, S. I.; Lever, A. B. P.; Grätzel, M. *Inorg. Chem.* **2002**, *41*, 367−378.

(18) Li, X. Y.; Long, N. J.; Clifford, J. N.; Campbell, C. J.; Durrant, J. R. *New J. Chem.* **2002**, 1076−1080.

(19) Zakeeruddin, S. M.; Nazeeruddin, M. K.; Humphry-Baker, R.; Péchy, P.; Quagliotto, P.; Barolo, C.; Viscardi, G.; Grätzel, M. *Langmuir* **2002**, *18*, 952−954.

(20) Hara, K.; Kurashige, M.; Dan-oh, Y.; Kasada, C.; Shinpo, A.; Suga, S.; Sayama, K.; Arakawa, H. *New J. Chem.* **2003**, 783−785.

(21) Hara, K.; Sato, T.; Katoh, R.; Furube, A.; Ohga, Y.; Shinpo, A.; Suga, S.; Sayama, K.; Sugihara, H.; Arakawa, H. *J. Phys. Chem. B* **2003**, *107*, 597−606.

(22) O'Regan, B.; Lenzmann, F.; Muis, R.; Wienke, J. *Chem. Mater.* **2002**, *14*, 5023−5029.

(23) Kumara, G. R. A.; Konno, A.; Shiratsuchi, K.; Tsukahara, J.; Tennakone, K. *Chem. Mater.* **2002**, *14,* 954−955.

(24) Bach, U.; Lupo, D.; Comte, P.; Moser, J. E.; Weissörtel, F.; Salbeck, J.; Spreitzer, H.; Grätzel, M. *Nature* **1998**, *395*, 583−586.

(25) Krüger, J.; Plass, R.; Grätzel, M.; Matthieu, H. J. *Appl. Phys. Lett.* **2002**, *81*, 367−369.

(26) Cao, F.; Oskam, G.; Searson, P. C. *J. Phys. Chem.* **1995**, *99*, 17071−17073.

(27) Nogueira, A. F.; Durrant, J. R.; De Paoli, M. A. *Adv. Mater.* **2001**, *13*, 826−830.

(28) Stathatos, E.; Lianos, P.; Lavrencic-Stangar, U.; Orel, B. *Adv. Mater.* **2002**, *14*, 354−357.

(29) Kubo, W.; Kitamura, T.; Hanabusa, K.; Wada, Y.; Yanagida, S. *Chem. Commun.* **2002**, 374−375.

(30) Wang, P.; Zakeeruddin, S. M.; Comte, P.; Exnar, I.; Grätzel, M. *J. Am. Chem. Soc.* **2003**, *125*, 1166−1167.

(31) Wang, P.; Zakeeruddin, S. M.; Moser, J. E.; Nazeeruddin, M. K.; Sekiguchi, T.; Grätzel, M. *Nat. Mater.* **2003**, *2*, 402−407.

(32) Bonhôte, P.; Dias, A. P.; Armand, M.; Papageorgiou, N.; Kalya-nasundaram, K.; Grätzel, M. *Inorg. Chem.* **1996**, *35*, 1168−1178.

(33) Finklea, H. O. In *Electroanalytical Chemistry*; Bard, A. J., Rubinstein, I., Eds.; Marcel Dekker: New York, 1996; Vol. 19, pp 108−335.

(34) Feldberg, S.; Rubinstein, I. *J. Electroanal. Chem.* **1988**, *240*, 1−15.

(35) Gu, G. Y.; Bouvier, S.; Wu, C.; Laura, R.; Rzeznik, M.; Abraham, K. M. *Electrochim. Acta* **2000**, *45*, 3127.

(36) Bard, A. J.; Faulkner, L. R., *Electrochemical Methods: Fundamentals and Applications*, 2nd ed; Wiley: Weinheim, 2001.

(37) Huang, S. Y.; Schlichthörl, G.; Nozik, A. J.; Grätzel, M.; Frank, A. J. *J. Phys. Chem. B* **1997**, *101*, 2576−2582.

(38) Vittadini, A.; Seloni, A.; Rotzinger, F. P.; Grätzel, M. *Phys. Rev. Lett.* **1998**, *14*, 2744−2747.

(39) Grätzel, M. *Prog. Photovoltaics* **2000**, *8*, 171−185.